Energy & Environmental Science

Supporting Information

Microstructural Iterative Reconstruction toward Excellent Thermoelectric Performance in MnTe

Yiyuan Luo,[1,#] Jinghan Wang,[1,#] Jianmin Yang,[1,#] Dasha Mao,[1] Juan Cui,[3] Baohai Jia,[1] Xusheng Liu,[4] Kornelius Nielsch,[2] Xiao Xu,[2,*] and Jiaqing He[1,*]

[1]Department of Physics, Southern University of Science and Technology, Shenzhen 518055, P. R. China

[2]Institute for Metallic Materials, Leibniz Institute for Solid State and Materials Research, Dresden 01069, Germany

[3]Laboratory of Computational Physics, Institute of Applied Physics and Computational Mathematics, Beijing 100088, P. R. China

[4]Shenzhen Institute for Advanced Study, University of Electronic Science and Technology of China, Shenzhen 518110, P. R. China

[#]These authors contributed equally

*Correspondence: X. Xu (x.xu@ifw-dresden.de), and J.Q. He (he.jq@sustech.edu.cn)

Contents

Experimental Section:

Sample preparation.

Polycrystalline MnTe, $MnSb_2Te_4$ and $Mn_{1-x}Ge_xSb_2Te_4$ (x= 0.02, 0.04, 0.05 and 0.06) were synthesized by the optimized vacuum melting method followed spark plasma sintering (SPS) method. Firstly, the commercial raw materials, Mn metal basis (10 mm & down, 5N, Alfa Aesar), Ge metal basis (3-9 mm, 5N, Alfa Aesar), Sb shot (1-3 mm, 6N, Alfa Aesar), and Te metal basis (zone refined, 6N, Alfa Aesar) were weighed stoichiometrically, then sealed in a type of double-layer tubes. The outer one is the quartz tube, which can suffer the heat near 1500 K. The inner one is the graphite tube which can avoid the reaction of Mn elements with the conventional quartz tube. Subsequently, the vacuumed tubes were heated up to 673 K and maintained for 2h, then, lifted to 1323 K and steadied for 2 days. Secondly, the complete mixed liquid phases were quenched and the as-obtained ingots were annealed at 873 K for 2 days, then, hand-milled for 30 minutes. Lastly, the as-obtained powders were sintered (SPS-211LX) with a parameter of Φ 10 mm, 50 MPa, and 823 K. Sb_2Te_3 and n type $Pb_{1-x}Sb_xTe$ samples were fabricated according to the references.[1,2]

Structural characterization.

The powder X-ray diffraction (XRD) results of all samples were conducted by a commercial instrument (Rigaku, Smartlab 9KW) from 10° to 80°. The Copper radiation with Kα = 1.5418 Å was equipped. The second phase images of the fracture appearances and the analysis of the joint interfaces were studied by a scanning electron microscope (Zeiss, Merlin) with an energy-dispersive spectroscopy (EDS)

probe. TEM samples were prepared by conventional mechanical polishing followed by argon ion milling (Gatan PIPS 695). Atomic structures of these samples were investigated by high angle annular dark-field (HAADF) in STEM model on a double Cs-corrected TEM (Thermo Fisher Scientific Themis G2 60-300) operated at 300 kV. The convergence angle and the collection angle for STEM imaging are 25 mrad and 48–200 mrad, respectively. Atomic-scale STEM-EDX mappings were generated in Velox (v2.12) with the radial wiener filter to enhance the feature of elemental maps.

Transport property characterization.

According to the texture analysis, all the sintered samples were cut parallel to the uniaxial pressure direction (as shown in Figure S3). The bar samples with a size of ~ 3 × 3 × 10 mm^3 were prepared to characterize the electrical conductivity (σ) and Seebeck coefficient (S), simultaneously. The uncertainty of each parameter of the commercial instrument (ZEM-3 M10, Ulvac Riko) was given as ~ 7%. The wafer samples with a size of Φ 10mm and thickness < 1 mm were cut for the Hall coefficient (R_H) measurement (Lake Shore 8400 Series). Consequently, the carrier concentration and mobility could be estimated by $n_H = 1/(eR_H)$ and $\mu_H = \sigma R_H$, respectively. The uncertainty was ~ 10%. The total thermal conductivity could be determined by $\kappa = DC_p d$, where D is the diffusivity, C_p is the specific heat capacity, and d is the sample density. The wafer samples with a size of Φ 10mm and thickness ~ 1.5 mm were cut to measure the temperature dependent D (LFA457, Netzsch). The given uncertainty of the commercial instrument was < 5%. C_p could be calculated by the Dulong-petit law,[3] and d was measured by the Archimedes' method (Table S1).

The total uncertainty of the thermal transport property part was ~ 10%. The longitudinal and transverse sound velocities were measured at 300K by the ultrasonic pulse-echo method (Olympus 5073PR pulser/receiver) with a 5MHz transducer and displayer (Tektronix MDO3054), as shown in Table S2.

DFT calculation.

To better understand the properties of $MnSb_2Te_4$, density functional calculations were performed using the program VASP[4] by the projector-augmented wave method[5] with the Perdew-Burke-Ernzerhof (PBE) generalized gradient approximation.[6] Van der Waals (VdW) interactions under the framework of the VdW-DF method with the optB86b-VdW exchange functional[7] were considered. A plane wave cutoff energy of 500 eV, a convergence criterion of 10^{-6} eV and a k-point mesh density of $2\pi\times$ 0.03 $Å^{-1}$ using the Γ-centered Monkhorst-Pack scheme[8] were used for calculations. The spin-orbit coupling (SOC) effect was included in the electronic structure calculations. The phonon dispersions and phonon density of states were calculated using the finite displacement method with the help of PHONOPY package,[9] where the primitive cell was enlarged to a 2×2×2 supercell.

To better understand the enhancement of hole mobility in Ge-doped $MnSb_2Te_4$, a 2×2×1 supercell with 84 atoms was constructed with 1 Mn atom substituted by the Ge atom, corresponding to a doping concentration of 8.3%. The structure was fully relaxed before the calculation of charge density, electron localization function (ELF) and density of states (DOS). The effective band structures of the undoped and doped

supercells were calculated using the band unfolding technique,[10] and the electrical conductivities were calculated based on the Boltzmann transport equation,[11]

$$\sigma = e^2 \int \Xi(\varepsilon)\left(-\frac{\partial f_0}{\partial \varepsilon}\right)d\varepsilon \quad \text{Equation (S1)}$$

where e, f_0 and ε are the electron charge, Fermi-Dirac distribution and energy eigenvalue, respectively. $\Xi(\varepsilon)$ is the transport distribution function, which is given by,

$$\Xi(\varepsilon) = \frac{1}{V}\sum_k v_{i,k}^2 \tau_{i,k} \quad \text{Equation (S2)}$$

where V is the unit cell volume and $v_{i,\boldsymbol{k}}$ and $\tau_{i,\boldsymbol{k}}$ are the group velocity and relaxation time of the i-th band at wavevector $\boldsymbol{k}$, respectively. In this study, the constant relaxation time approximation was applied and relaxation times in the range of 5~10 fs were used.

The decrease of hole concentration in Ge doped sample could be explained by the defect formation energy of Mn vacany (E^f of V_{Mn}), which is defined as,[12]

$$E^f\left(V_{Mn}^q\right) = E_{tot}\left(V_{Mn}^q\right) - E_{tot}(bulk) + \mu_{Mn} + qE_F + E_{corr} \ldots \quad \text{Equation (S3)}$$

where $E_{tot}\left(V_{Mn}^q\right)$ and $E_{tot}(bulk)$ are the total energies of the defective and the perfect supercell, respectively; E_F and E_{corr} are the Fermi energy and the correction term, respectively. μ_{Mn} represents the chemical potential of Mn, which equals the energy of one Mn atom in its bulk phase, and q represents the charge state of the defect; To omit the E_{corr}, a large 3×3×1 supercell including 189 atoms was constructed. Since the bandgap of pristine $MnSb_2Te_4$ is very narrow, we calculated the formation energy by setting the Fermi energy equals the valence band maximum energy.

Module preparation.

The module with a bottom area of 20 × 20 mm^2 were assembled by 8 pairs of p-type ($Mn_{0.96}Ge_{0.04}Sb_2Te_4$) and n-type ($Pb_{0.985}Sb_{0.015}Te$) legs. Firstly, p- and n-type materials were sintered with a size of Φ 20 mm and thickness ~ 12 mm. Then, the ingots were cut by a multi-wire diamond saw with a leg bottom area of ~ 3.5 × 3.5 mm^2. A type of Ni-based barrier layer was electroplated to the as-obtained legs, and the thicknesses were checked by the SEM analysis. Thus, the prepared legs were soldered with the copper-clad pate by the commercial tin-based high-temperature solder. To ensure the repeatability, a second module with a height of ~ 13 mm was assembled. The as-obtained $Mn_{0.96}Ge_{0.04}Sb_2Te_4/Pb_{0.985}Sb_{0.015}Te$ module was characterized by a commercial instrument (PEM-2, Riko), and a stable cold side temperature of 293 K was set. The hot side temperature dependence of voltage, power and efficiency could be measured. Because the efficiency is estimated by $P/(P+Q_c)$, here, the cold side heat flow Q_c is deeply related to the accuracy of the results from the thermocouples, considering the influence of radiant heat, the device uncertainty could be ~ 20% when hot side temperature is higher than 600 K.[13] The size of measuring platform of the commercial instrument was set as 20 × 20 mm^2, and a type of asbestos blanket was employed as the heat insulator to reduce the radiant heat in $MnSb_2Te_4$-based module. The performance of second module was depicted in Figure S12, insert is the measured two modules.

The single parabolic band (SPB) calculation:

In the case of strong degeneracy situation, a SPB model[14,15] can be employed to describe the linear relationship of S and n_H,

$$S = \frac{8\pi^2 k_B^2 T}{3eh^2} m_d^* \left(\frac{\pi}{3n_H}\right)^{2/3} \quad \text{Equation (S4)}$$

where k_B is the Boltzmann constant, e is the electron charge, and h is the Plank's constant.

On the basis of SPB model, the Lorenz number can be further calculated from the following equations,

$$S = \pm \frac{k_B}{e}\left(\frac{\left(\lambda+\frac{5}{2}\right)F_{\lambda+\frac{3}{2}}(\eta)}{\left(\lambda+\frac{3}{2}\right)F_{\lambda+\frac{1}{2}}(\eta)} - \eta\right) \quad \text{Equation (S5)}$$

$$F_n(\eta) = \int_0^\infty \frac{x^n}{1+e^{x-\eta}} dx \quad \text{Equation (S6)}$$

$$L = \left(\frac{k_B}{e}\right)^2 \left\{\frac{\left(\lambda+\frac{7}{2}\right)F_{r+\frac{5}{2}}(\eta)}{\left(\lambda+\frac{3}{2}\right)F_{r+\frac{1}{2}}(\eta)} - \left[\frac{\left(\lambda+\frac{5}{2}\right)F_{r+\frac{3}{2}}(\eta)}{\left(\lambda+\frac{3}{2}\right)F_{r+\frac{1}{2}}(\eta)}\right]^2\right\} \quad \text{Equation (S7)}$$

where λ is the scattering parameter which equals to -0.5 for acoustic phonon scattering, $F_n(\eta)$ is the n-th order Fermi integral and η is the reduced Fermi energy, which can be calculated from the experimental S values.

The predicted PF value can be derived from above calculating results as $PF = S^2\sigma = S^2 n_H e \mu_H$.

The supplementary images

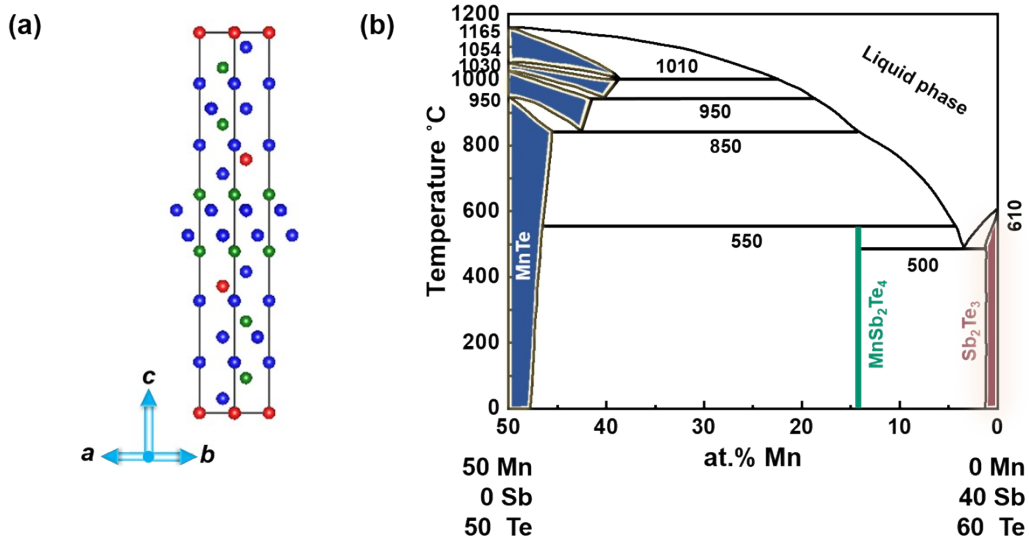

Figure S1. (a) The unit cell of $MnSb_2Te_4$. (b) The rebuilt phase diagram of $MnSb_2Te_4$ based on the reference.[16,17]

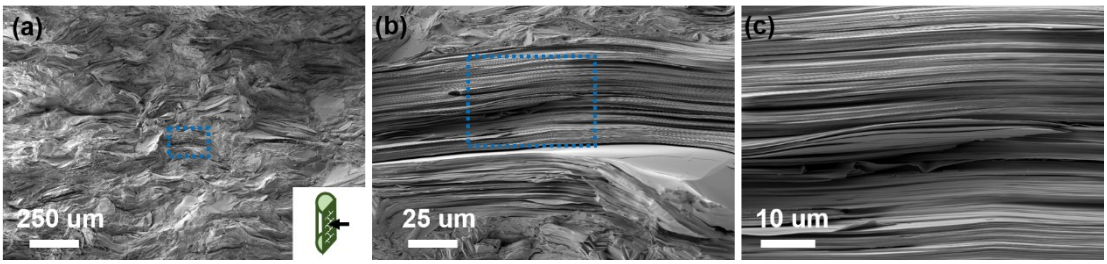

Figure S2. (a) The fracture appearance of the $MnSb_2Te_4$ polycrystal, insert is the schematic of fracture plane and the beam direction; (b) the magnified image of corresponding area in (a), marked as blue rectangle; (c) the magnified image of corresponding area in (b), marked as blue rectangle.

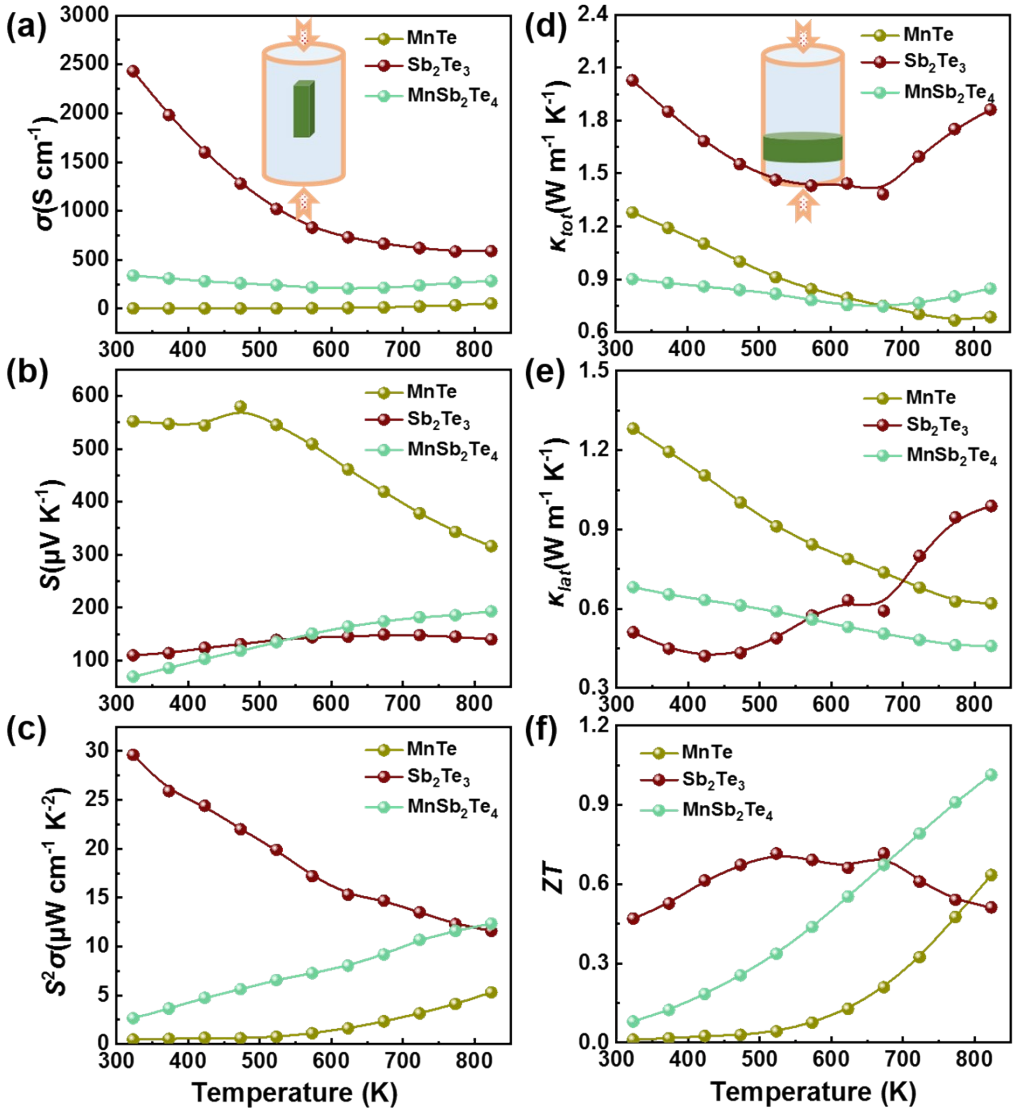

Figure S3. The temperature dependent (a) σ, (b) S, (c) PF, (d) κ_{tot}, (e) κ_{lat} and (f) ZT of MnTe, Sb_2Te_3, and $MnSb_2Te_4$ samples, respectively. Inserting images depict the measured direction.

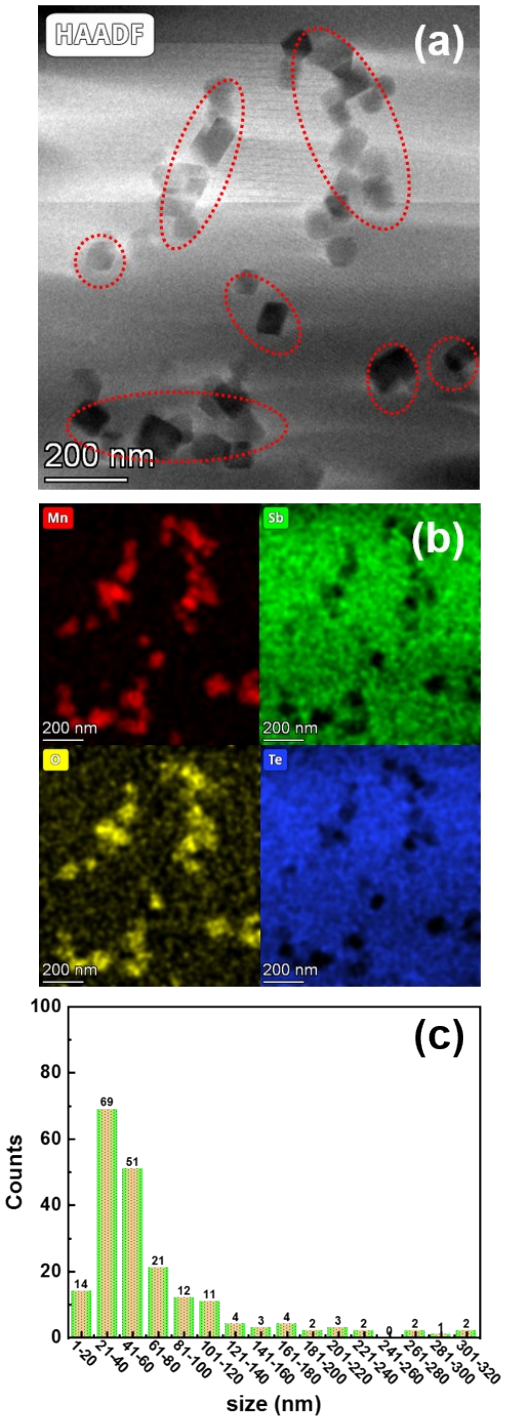

Figure S4. (a) The low magnification HAADF-STEM image of $MnSb_2Te_4$ sample; (b) the EDS analysis of corresponding area. (c) The statistical data of the precipitate size from a large distribution scale in $MnSb_2Te_4$.

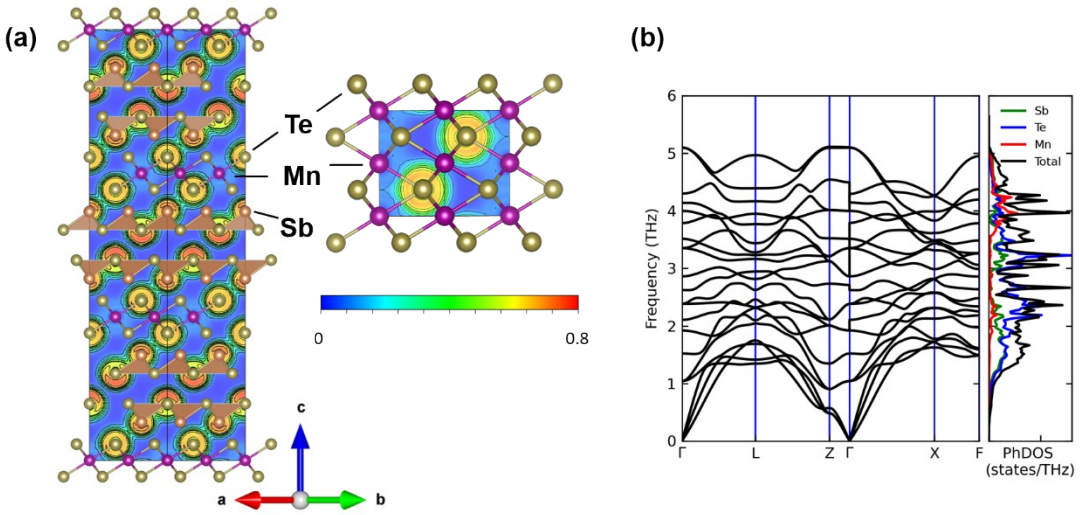

Figure S5. (a) The electron localization function (ELF) of $MnSb_2Te_4$ and MnTe. (b) The phonon dispersion and partial phonon density of states (PhDOS) of $MnSb_2Te_4$.

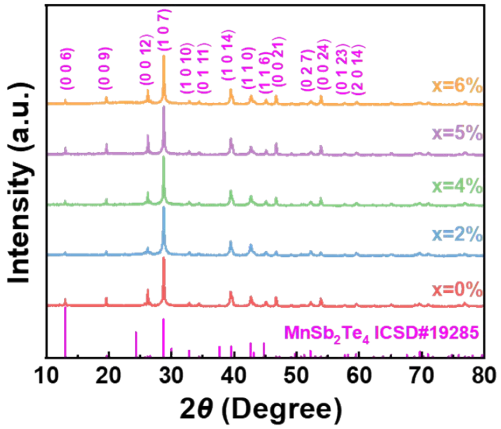

Figure S6. The XRD pattern of $Ge_{1-x}Mn_xSb_2Te_4$ samples (x = 0, 0.02, 0.04, 0.05, and 0.06), respectively.

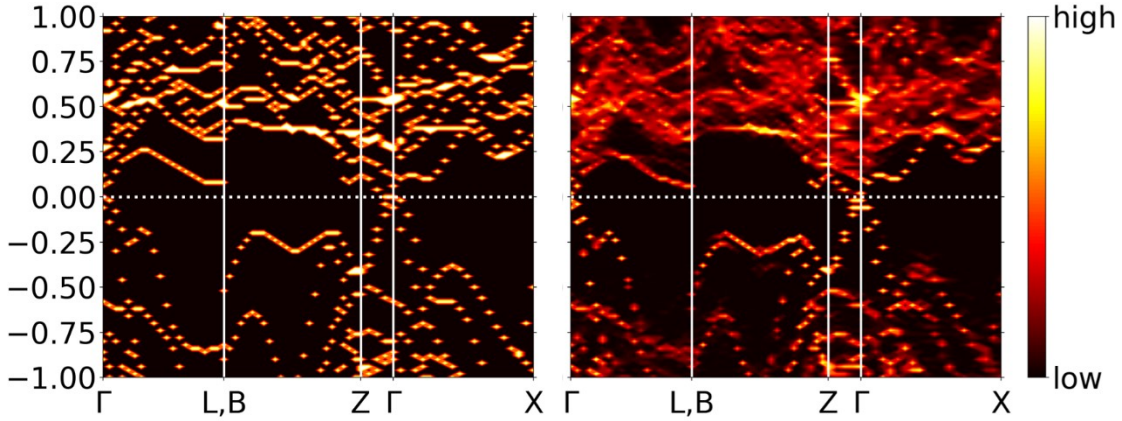

Figure S7. The effective band structures of pristine $MnSb_2Te_4$ (left) and Ge-doped $MnSb_2Te_4$ (right).

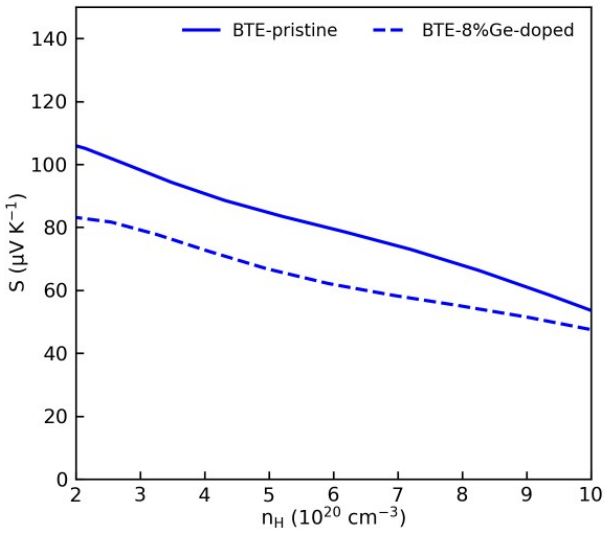

Figure S8. The simulated Seebeck coefficients of $MnSb_2Te_4$ and $Mn_{11}GeSb_{24}Te_{48}$. The S decreases after doping due to the decrease of DOS m^*, which agree with the experimental pisarenko plot.

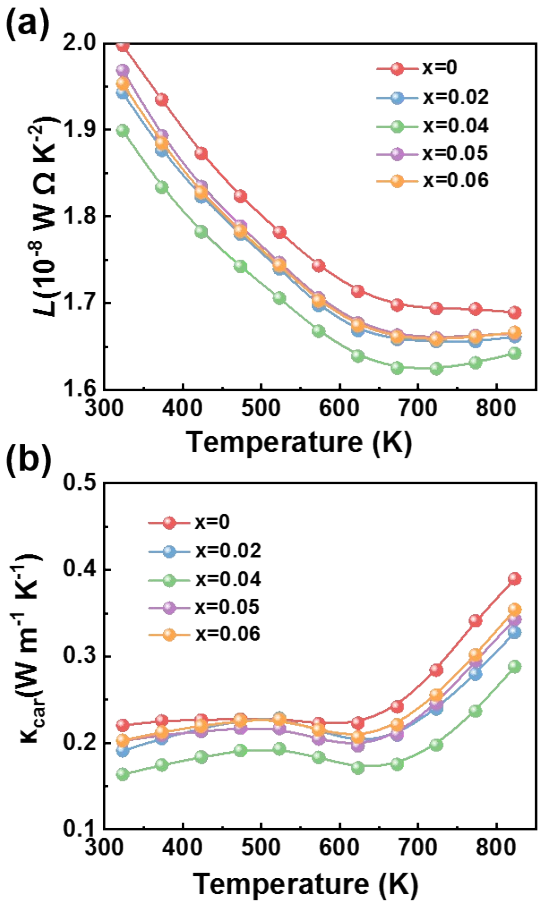

Figure S9. The temperature dependence of L number and κ_{car} of $Ge_{1-x}Mn_xSb_2Te_4$ samples (x = 0, 0.02, 0.04, 0.05, and 0.06), respectively.

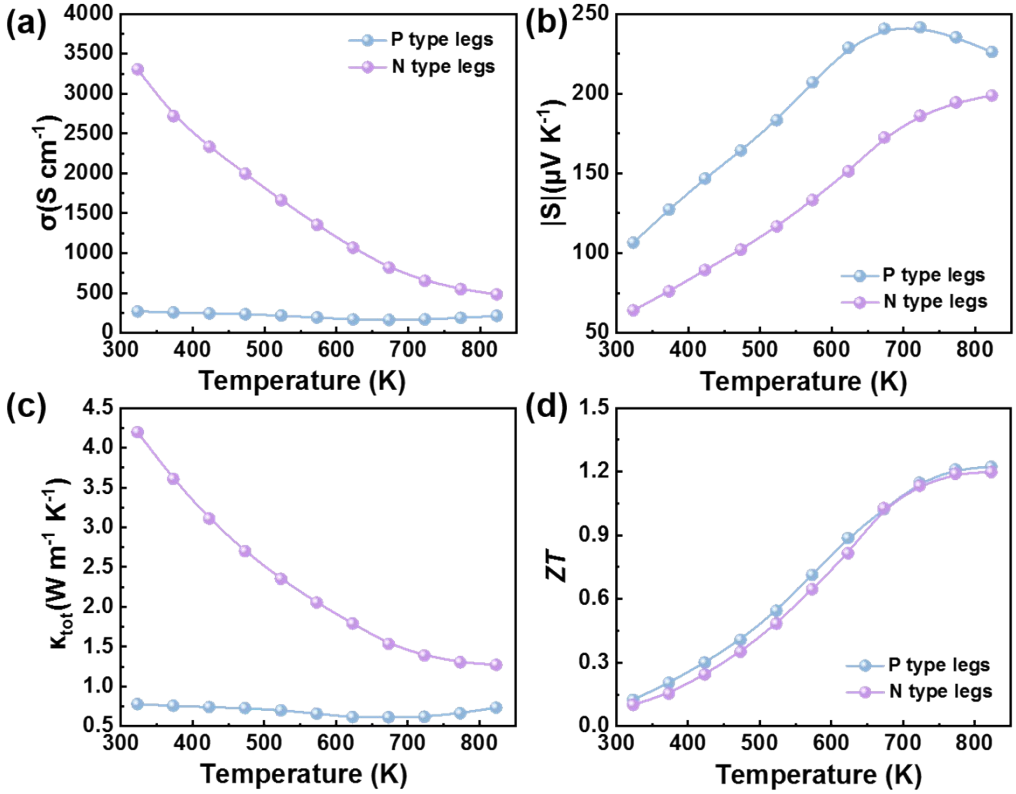

Figure S10. The temperature dependence of (a) electrical conductivity, (b) Seebeck coefficient, (c) total thermal conductivity, and (d) *ZT* value of p- and n-type leg materials.

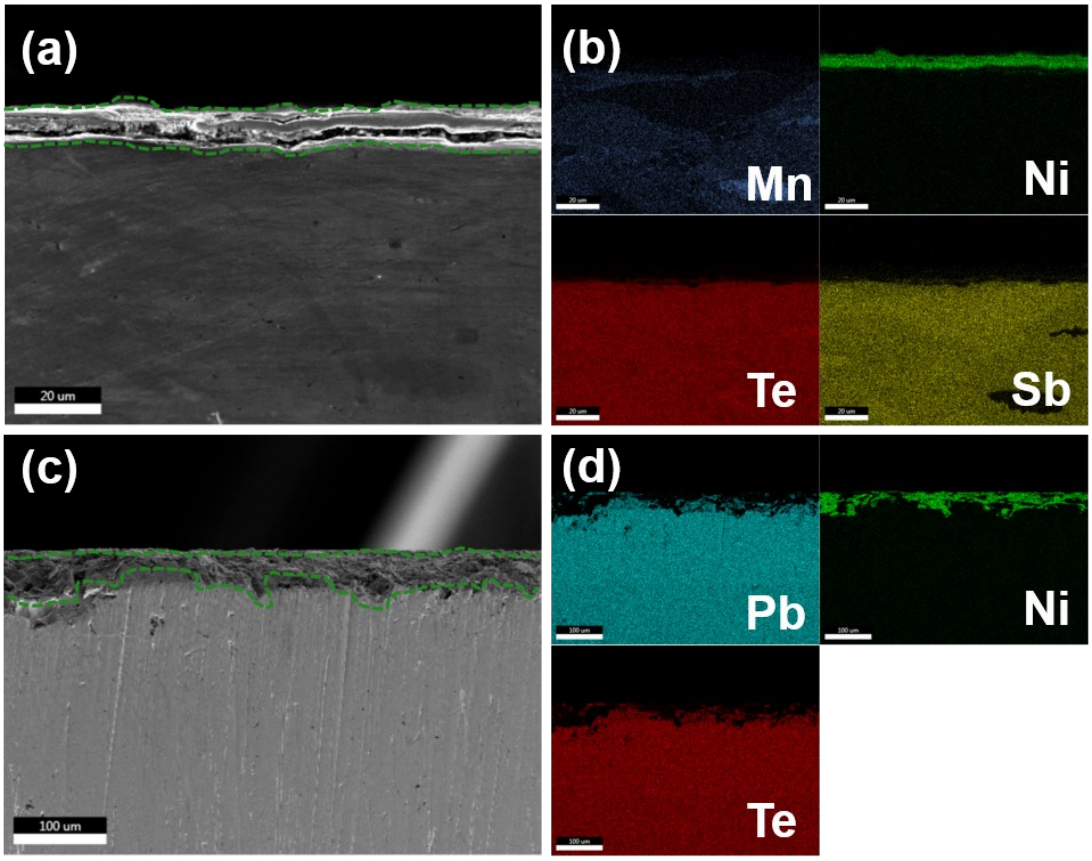

Figure S11. (a) The SEM image of the top of p-type leg and (b) the EDS mapping of the corresponding region. (c) The SEM image of the top of n-type leg and (d) the EDS mapping of the corresponding region. The thicknesses of the electroplated Ni layers are estimated averagely according to the green dash lines.

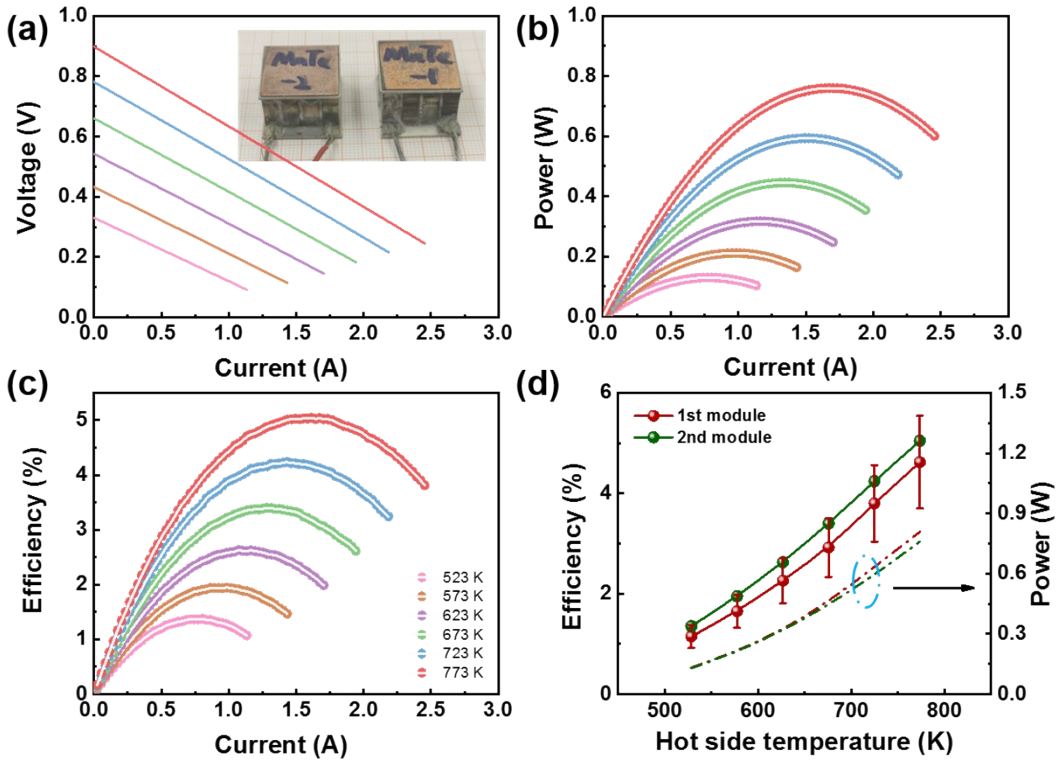

Figure S12. The current dependence of (a) voltage, (b) power, and (c) efficiency under different hot-side temperature, respectively. Insert is the optical image of measured two modules. (d) Comparison of the measured efficiency and power of our first and second modules.

The supplementary images

Table S1. Mass densities ρ(g/cm3) of all samples

Compositions	***ρ*(g/cm^3)**	**Compositions**	***ρ*(g/cm^3)**
MnTe	5.8451	$Mn_{0.98}Ge_{0.02}Sb_2Te_4$	6.2644
Sb_2Te_3	6.1885	$Mn_{0.96}Ge_{0.04}Sb_2Te_4$	6.2838
$MnSb_2Te_4$	6.2723	$Mn_{0.95}Ge_{0.05}Sb_2Te_4$	6.3099
		$Mn_{0.94}Ge_{0.06}Sb_2Te_4$	6.3209

Table S2. Sound velocity of MnTe-based samples

Compositions	v_s (m s^{-1})	v_l (m s^{-1})	v_a (m s^{-1})
MnTe	1803.47	3485.91	2018.90
$MnSb_2Te_4$	1799.20	3237.41	2003.81
$Mn_{0.98}Ge_{0.02}Sb_2Te_4$	1797.05	3276.28	2003.45
$Mn_{0.96}Ge_{0.04}Sb_2Te_4$	1703.32	3192.71	1902.83
$Mn_{0.95}Ge_{0.05}Sb_2Te_4$	1838.27	3348.54	2049.28
$Mn_{0.94}Ge_{0.06}Sb_2Te_4$	1788.54	3202.67	1991.17

References

(1) Fu, L.; Yin, M.; Wu, D.; Li, W.; Feng, D.; Huang, L.; He, J. *Energy Environ. Sci.* **2017**, *10*, 2030-2040.

(2) Wu, H.; Sun, Y.; Wang, Y.; Qin, H.; Zhu, J.; Zhu, Y.; Hu, J.; Guo, M.; Liu, J.; Liu, M.; Guo, F.; Zhang, Q.; Liu, Z.; Cai, W.; Sui, J. *Mater. Today Energy* **2022**, *27*, 101045.

(3) Dong, J.; Pei, J.; Hayashi, K.; Saito, W.; Li, H.; Cai, B.; Miyazaki, Y.; Li, J. F. *J. Materiomics* **2021**, *7*, 577-584.

(4) Kresse, G.; Furthmüller, J. *Phys. Rev. B* **1996**, *54*, 11169-11186.

(5) Blöchl, P. E. *Phys. Rev. B* **1994**, *50*, 17953-17979.

(6) Perdew, J. P.; Burke, K.; Ernzerhof, M. *Phys. Rev. Lett.* **1996**, *77*, 3865-3868.

(7) Klimeš, J.; Bowler, D. R.; Michaelides, A. *Phys. Rev. B* **2011**, *83*, 195131.

(8) Monkhorst, H. J.; Pack, J. D. *Phys. Rev. B* **1976**, *13*, 5188-5192.

(9) Togo, A.; Tanaka, I. *Scripta Mater.* **2015**, *108*, 1-5.

(10) Popescu, V.; Zunger, A. *Phys. Rev. B* **2012**, *85*, 085201.

(11) Madsen, G. K. H.; Carrete, J.; Verstraete, M. J. *Comput. Phys. Commun.* **2018**, *231*, 140-145.

(12) Freysoldt, C.; Grabowski, B.; Hickel, T.; Neugebauer, J.; Kresse, G.; Janotti, A.; Van de Walle, C. G. *Rev. Mod. Phys.* **2014**, *86*, 253-305.

(13) Yan, Q.; Kanatzidis, M. G. *Nature Mater.* **2022**, *21*, 503-513.

(14) Yang, J.; Xi, L.; Qiu, W.; Wu, L.; Shi, X.; Chen, L.; Yang, J.; Zhang, W.; Uher, C.; Singh, D. J. *npj Comput. Mater.* **2016**, *2*, 15015.

(15) Xu, X.; Huang, Y.; Liu, X.; Jia, B.; Cui, J.; He, R.; Wang, J.; Luo, Y.; Nielsch, K.; He, J. *Energy Environ. Sci.* **2022**, *15*, 4058-4068.

(16) Noor, S. S. A. *J. Appl. Phys.* **1987**, *61*, 3549-3551.

(17) Yan, J. Q.; Okamoto, S.; McGuire, M. A.; May, A. F.; McQueeney, R. J.; Sales, B. C. *Phys. Rev. B* **2019**, *100*, 104409.